



HAL
open science

Degradation by hydrolysis of three triphenylmethane dyes: DFT and TD-DFT study

Djamel Taharchaouche, Nadjia Latelli, Hafida Merouani, Boussebbat Wahiba, Naima Mechehoud, Nadia Ouddai, Christophe Morell, Lynda Merzoud, Henry Chermette

► **To cite this version:**

Djamel Taharchaouche, Nadjia Latelli, Hafida Merouani, Boussebbat Wahiba, Naima Mechehoud, et al.. Degradation by hydrolysis of three triphenylmethane dyes: DFT and TD-DFT study. *Theoretical Chemistry Accounts: Theory, Computation, and Modeling*, 2023, 142 (1), pp.10. 10.1007/s00214-022-02950-1 . hal-03917879

HAL Id: hal-03917879

<https://cnrs.hal.science/hal-03917879>

Submitted on 2 Jan 2023

HAL is a multi-disciplinary open access archive for the deposit and dissemination of scientific research documents, whether they are published or not. The documents may come from teaching and research institutions in France or abroad, or from public or private research centers.

L'archive ouverte pluridisciplinaire **HAL**, est destinée au dépôt et à la diffusion de documents scientifiques de niveau recherche, publiés ou non, émanant des établissements d'enseignement et de recherche français ou étrangers, des laboratoires publics ou privés.

Degradation by hydrolysis of three triphenylmethane dyes: DFT and TD-DFT study.

Djamel Taharchaouche^{a, b}, Nadjia Latelli^{*, a, b}, Hafida Merouani^{b, c}, Boussebbat Wahiba^b, Naima Mechehoud^b, Nadia Ouddai^b, Christophe Morell^d, Lynda Merzoud^d, Henry Chermette^{*, d}

a Faculté des sciences, département de chimie, Université de Msila, BP 166 Ichbilia, 28000 M'sila, Algeria

b Laboratoire chimie des matériaux et des vivants : activité, réactivité, Université El-Hadj Lakhdar Batna1, 05001 Batna, Algeria

c Faculté des Technologies, département de science technique, Université de Batna 2.

d Université de Lyon; Université Lyon 1 et CNRS UMR 5280, Institut des Sciences Analytiques, 5 rue de la Doua, 69100 Villeurbanne, France

Abstract: DFT reactivity descriptors, the ultraviolet-visible spectra and hydrolysis mechanism of three cationic dyes (Malachite Green (MG), Brilliant Green (BG) and Ethyl Green (EG)) are performed with several exchange-correlation functional (global GGA, hybrids and range-separated). Using time-dependent density functional theory the theoretical ultraviolet-visible absorption spectra of the three cationic dyes are obtained and obey the trend for the λ_{\max} : GGA > hybrid > range-separated functional. Thanks to the transition state theory, the barriers of hydrolysis mechanism of the cation structures dyes were obtained in gas and solution phase. It is shown that, for these systems the barriers are in order: $BG^+ < MG^+ < EG^{2+}$ in gas and solution phase. In the two phases, the CAM-B3LYP functional gives the highest barriers and the M06 gives the lowest ones.

Keywords: dye; Triphenylmethane; DFT; TD-DFT; degradation

1. Introduction

Triphenylmethane dyes and their heterocyclic derivatives are the oldest class of synthetic dyes. They have retained a wide commercial value, as they cover the entire visible spectrum. The intense coloring of triphenylmethane derivatives come from the large conjugate system of the cationic ion. The central carbocation is conjugated with three benzene rings, where the positive charge is strongly relocated [1]

The degradation of dyes has been investigated in several experimental studies [2,3]. The malachite green dye, which is the most famous among the triphenylmethane dyes has been widely studied [4 -12]. Most of these experimental studies have suggested that the $\cdot\text{OH}$ radical attacks preferentially the central carbon of this dye. The study reported by Navarro et al. [13] proposed that the degradation mechanism is initiated by the attack of hydroxyl radicals onto the central carbon of malachite Green (MG). This attack generates 4-(dimethylamino) benzophenone (DLBP) followed by the addition of hydroxyl radicals to the non-amino aromatic ring of DLBP and the demethylation of the amino group [13].

Recently, some theoretical papers have been proposed to study the triphenylmethane dyes [14-18]. Guillaumont and Nakamura [14] used the TD-DFT method to calculate the absorption wavelengths and oscillator strengths in the Franck-Condon region of a series of organic dyes important for the dye industry (indigo, azobenzene, phenylamine, hydrazone, anthraquinone, naphthoquinone and cationic dyes). Moreover, Preat et al.[15] have also used the TD-DFT method to evaluate the absorption spectra of arylcarbonium ion derivatives in acetic acid.

Other studies undertaken by Rafiq et al.[16] exploited the TD-DFT method to roughly scan the S_2 , S_1 , and S_0 potential energy profiles along the torsional coordinates of phenyl rings.

Nakayama and Taketsugu [17] investigated the nonradiative deactivation process of malachite green in the singlet excited states, S_1 and S_2 , by high-level ab initio quantum chemical calculations using the CASPT2//CASSCF approach. In 2015, Xie et al. [18] employed the semi empirical OM2/MRCI method to simulate the S_2 and S_1 photodynamics of malachite green.

The hydrolysis of these cationic dyes is less studied. A part of the present work will address the point. We found two experimental works dealing with the hydrolysis of the dyes studied. In a first work [19], the hydrolysis of Brilliant Green and some derivatives has been studied over the pH range 6-11. Brenda et al.[19] concluded that in neutral aqueous solution and in the absence of light, the system reaches an equilibrium and the initial rate of fading of Brilliant Green in neutral aqueous solution is much faster than the rate expected from the reaction with a hydroxide ion concentration of 10^{-7} mol dm⁻³. [19]

In a second work, Beach et al.[20] have measured the rate constants for the reaction of hydroxide ions with Crystal Violet, Ethyl Violet, Pyrrolidine Violet and the 2,20-isopropyl and oxygen bridged analogues of Crystal Violet. The authors have concluded that the rates of hydrolysis of dyes of the Crystal Violet type are substantially slower than those of the analogous Malachite Green dyes in accord with the additional stabilisation of the cation provided by the third terminal amino function. [20]

So before moving on to the study of the hydrolysis reactions of our substrates namely the (4 - [(4-dimethylaminophenyl) -phenyl-methyl] -N, N-dimethyl-aniline (Malachite Green MG), the 4 - [[4- (diethylamino) phenyl]-phenylmethylidene] cyclohexa-2,5-dien-1-ylidene] – diethylazanium hydrogen (Brilliant Green BG) and the [4-[[4-(dimethylamino)phenyl]-(4 dimethylazaniumylidenecyclohexa-2,5-dien-1-ylidene)methyl]phenyl]-ethyl

experimental data. Before concluding, in section IV, the hydrolysis reactions mechanism of these cationic dyes is studied. In all along the work, the importance of the DFT exchange-correlation functional is assessed.

2. Computational Details

All calculations were carried out at DFT level using the GAUSSIAN09 program package [21]. The structures were optimized without any restrictions at seven (7) levels of theory, namely GGA functional (PBE[22], BP86[23-25] hybrid functionals (B3LYP[26], M06[27], M06-2X[28]), PBE0 [29] and range-separated functionals CAM-B3LYP[30], ω B97X-D [31].

An all electron valence double-zeta basis augmented with one polarization function (6-31G(d)) has been retained for all atoms other than hydrogen [32]. For each system, the ground-state structure has been determined by a standard force-minimization process, and the vibrational spectrum has been determined to systematically check the absence of imaginary frequencies. All transition states have been characterized, corresponding to first order saddle points, i.e. with only one imaginary frequency. The incidence of the water solvation has been evaluated via the Polarizable Continuum Model (CPCM). [33,34] DFT calculations are used to evaluate the solvent effects model through single point DFT calculations, at the gas phase optimized geometry. Energy levels of the Highest Occupied Molecular Orbital (HOMO) and the Lowest Unoccupied Molecular Orbital (LUMO), as well as the chemical reactivity parameters were also obtained at ground state optimized geometry. TD-DFT calculations were carried with the same functionals in order to get straightforward conclusions of the global GGA, hybrid and range-separated functional on the reliability of the spectral predictions [35,36]. After geometry optimization, single point calculations were carried out in CPCM model. TD-DFT calculations were carried out in CPCM model to obtain the UV/VIS

spectra of the different dyes. The Gaussian 16 software package [37] is used to examine the nature of the excited state transitions by calculations of the charge-transfer distance index, D_{CT} , and the amount of charge transferred index Q_{CT} . [38]

3. Results and discussion

3.1 Dyes Structures.

After the selection of a DFT functional and basis set, the geometry is one parameter to investigate. The results of geometric parameters for three dyes calculated with global GGA, hybrid and range-separated functionals (PBE, BP86, B3LYP, M06, M06-2X, PBE0, CAM-B3LYP and ω B97X-D) are given in Table S-1 (SI). The atom-numbering and the obtained structures are displayed in Scheme 1. The Mulliken charges and the natural population charges obtained by NBO calculations are given in Table S-2 and Table S-3 respectively. Let us remind that the NBO calculations uses the second-order perturbation energies (2) from donor (i) to acceptor (j). By NBO calculations, we can estimate the electron density delocalization from the occupied Lewis-type (donor) NBOs to properly unoccupied non-Lewis-type (acceptor) NBOs within the molecule [39]. The optimized structures (Table S-1 ESI[†]) of three dyes compare well with the experimental ones of triphenylmethane, and tri-*p*-nitrophenylmethyl obtained by Andersen [40,41].

The C1-C2 and C1-C14 bond lengths calculated with seven functionals are equidistant for the MG⁺, BG⁺ and EG2⁺ dyes (See Table S-1). This is a consequence of the local symmetry. Both are shorter than their neighboring C1-C8 bond length. Note that, the C1-C2 and C1-C14 bond lengths are in between typical C–C single and double bonds, whereas the C1-C8 bond is a typical C–C single bond. [18] This can be understood in view of available resonance structures

of, for instance, MG in the S_0 state. The C-C bond distances within the three phenyl rings are in the range (1.379-1.435 Å; 1.365-1.431 Å; 1.364-1.429 Å with the global GGA, hybrids and range-separated functionals respectively) consistent with a bond order of 1.5, corresponding to delocalized π -systems. C-N bonds lengths lie in the (1.358-1.513 Å; 1.342-1.509 Å; 1.341-1.500 Å range with global GGA, hybrids and range-separated functionals, respectively) which agree with those estimated by Microwave spectra measurement (1.402(2) Å) [42]; The later are also compatible with the asymmetric unit in aniline, determined at 252 K, which contains two independent molecules with different C-N distances amounting 1.399(6) and 1.385(6) Å.[43] Generally, the average bond lengths calculated by the range-separated functional are systematically a little shorter than those by the hybrid and GGA functionals (see Table S-1). In agreement with [44] the central angles (C2C1C8, C2C1C14, and C8C1C14), do not differ significantly from the 119-120° experimental values.[40,41] This is a proof of the planarity of the group, and in agreement with a local D_{3h} symmetry of the triphenylmethane. Therefore, the N20 and N21 atoms are equivalent for the three dyes, Tables S-2 and S-3 show that these atoms hold the same charges.

3.2 DFT reactivity descriptors.

Using the energy levels of the highest occupied molecular orbital (HOMO) and the lowest unoccupied molecular orbital (LUMO), the chemical reactivity parameters [45] in the gas phase and solvent phase were calculated (in eV): chemical potential (μ), chemical hardness (η), electrophilicity index (ω), and dipole moment (D Debye). The values are shown in Tables S4 and S5. Typically, chemical hardness is an important parameter (difference between HOMO and LUMO) that represents the resistance to charge transfer;[46,47] hence, the highest chemical hardness is desired for stable compounds. A significant sensitivity to the

exchange-correlation functional can be observed, through higher LUMO values with range-separated functionals (CAM-B3LYP, ω B97X-D) than values with hybrid functionals (B3LYP, PBE0), themselves higher than values with GGA functionals (BP86, PBE, M06); the M06-2X providing results between those of the hybrids and the range-separated functionals. This behavior leads evidently to higher hardness values within range-separated functionals than with GGAs.

However, in this case, the EG2⁺ dye has a lower value of chemical hardness in both phases (See Tables 1, 2) than that of MG⁺ and BG⁺ dyes, which means that the EG2⁺ dye is more reactive than MG⁺ and BG⁺ dyes. This can be related to its +2 charge instead of +1.

To the best of our knowledge, there are not so many works relating the reactivity descriptors of triphenylmethane derivatives. Indeed, two papers appeared recently containing reactivity descriptor studies of some triphenylmethane dyes. **[48, 2]** In one of them **[48]**, El Haouti et al. studied experimentally the adsorption of two cationic dyes by Na-Montmorillonite Nano Clay, one of them belonging to the triphenylmethane family, namely the Cristal Violet. They also computed at B3LYP level a few global DFT descriptors μ , η and ω , and their results, at least the hardness, are quite compatible to our results, reported in Table 1. More precisely, one had to normalize their values of η and ω , since they used a wrong definition of formula of η . Moreover, their values of μ are significantly lower than ours, since their calculations were performed on neutral molecules instead of cations.

In the second paper, Bendjabeur et al. **[2]** used also the density functional theory (DFT) with the BP86 GGA functional to study the photolysis of three triphenylmethane dyes (basic

Fuchsin, acid Fuchsin and Gentian violet). The HOMO and LUMO energies, and related values in their work are compatible with our results obtained with GGA functionals (PBE and BP86).

1. 3.3.Ultraviolet-visible spectra of dyes.

Absorption wavelengths and oscillator strength (f), as well as the orbitals involved in the transitions in solvent with CPCM model are reported in Table 1 for the three closed-shell cationic dyes at the eight levels of theory. Because we want to compare with experiment, the theoretical spectra are calculated only within the solvent model. As is well known, for most studied systems the theoretical wavelength is just the first transition with significant oscillator strength [49-55], although first transition with a small oscillator strength may be visible through significant vibronic coupling. For the three systems studied here, this transition is just the HOMO \rightarrow LUMO one. The theoretical ultraviolet-visible absorption spectra of the three cationic dyes obtained at the same levels of theory are shown in Figures 1-3.

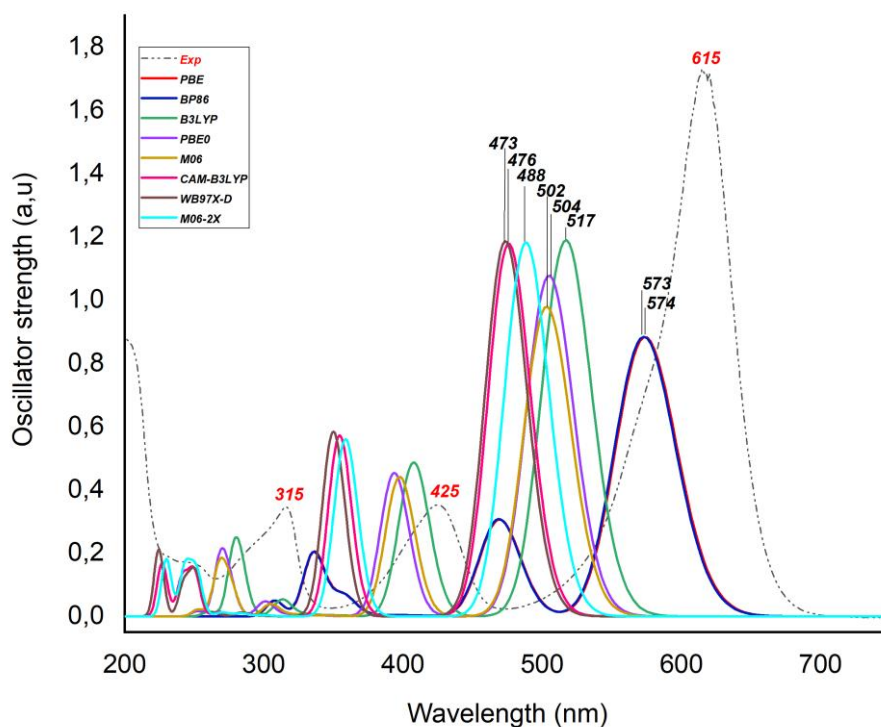


Figure 1: The experimental and theoretical UV-Visible spectra of MG^+ dye calculated in the solvent (CPCM model) (FWHM = 0.195 eV).

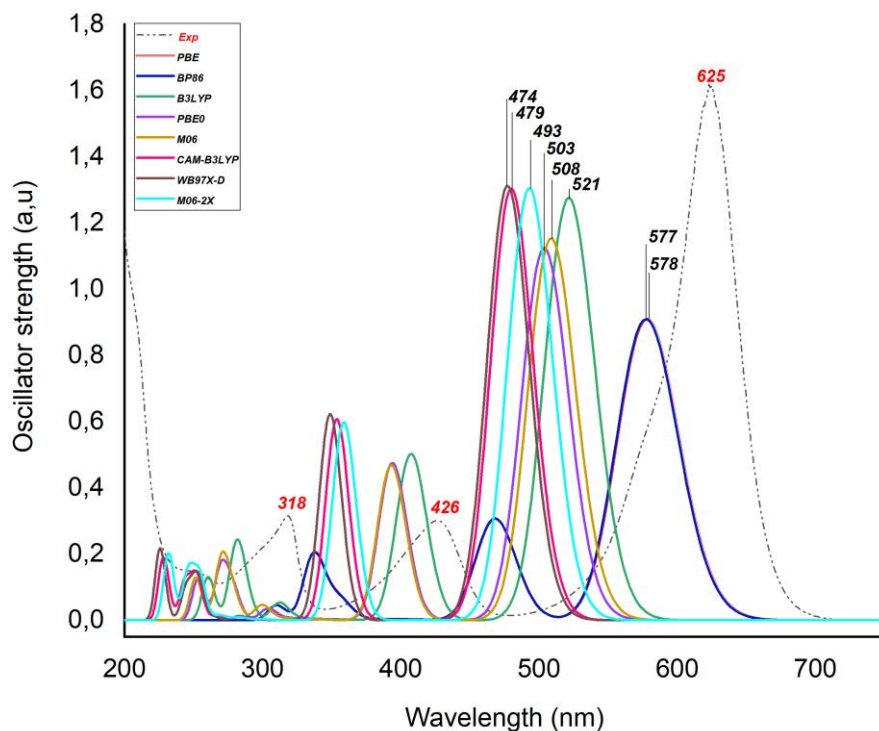


Figure 2: The experimental and theoretical UV-Visible spectra of BG^+ dye calculated in the solvent (CPCM model) (FWHM = 0.195 eV).

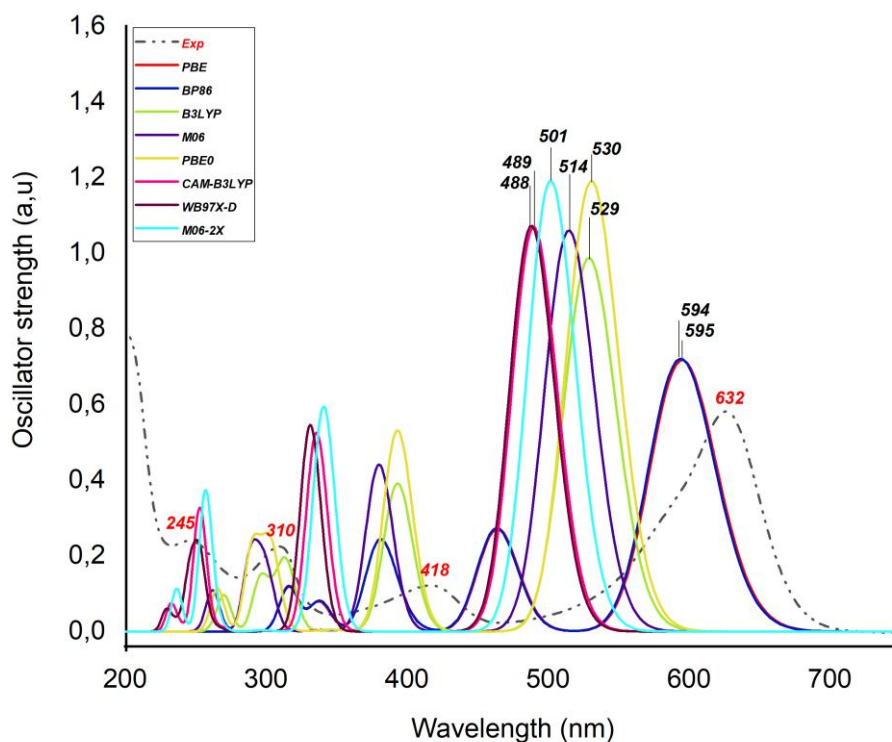


Figure 3: The experimental and theoretical UV-Visible spectra of EG^{2+} dye calculated in the solvent (CPCM model) (FWHM = 0.227 eV).

Firstly, the main bands appear in the visible region. Indeed, the electronic spectra of three dyes show resemblances in shapes and band positions (Figures 1-3 and Table 1)

For all compounds, the absorption wavelengths systematically obey the trend: PBE > BP86 > B3LYP > PBE0 > M06 > M06-2X > CAM-B3LYP > ω B97X-D. This can be summarized according to the class of functionals: GGA > hybrid > range-separated functionals. This confirms that the larger exact exchange ratio at intermediate r12 leads to the smaller calculated λ_{\max} as already shown in [56]. In several studies,[57-59] PBE0 yields λ_{\max} in very good agreement with experimental trends for the short-wavelength dyes. In our study the GGAs functional gives the largest λ_{\max} . This could be related to the fact that our dyes are cationic.

Table 1: Absorption wavelengths, oscillator strength (f), and the orbitals involved in the transitions of three dyes using eight levels of theory (CPCM model, nstates =20) H (HOMO), L (LUMO)

Dyes	Functionals	λ_{\max} (nm)	f	Transitions H=HOMO, L=LUMO (%)	Functionals	λ_{\max} (nm)	f	Transitions H=HOMO, L=LUMO (%)
MG ⁺	PBE	574	0.848	H→L (100%)	M06	502	0.988	H→L (100%)
		469	0.293	H-1→L (95%)		397	0.444	H-1→L (96%)
		335	0.175	H→L+2 (96%)		268	0.155	H→L+2 (90%)
	BP86	573	0.849	H→L (100%)	M06-2X	488	1.135	H→L (98%)
		468	0.295	H-1→L (95%)		358	0.538	H-1→L (94%)
		334	0.174	H→L+2 (96%)		243	0.147	H→L+2 (46%) H→L+4 (32%)
	B3LYP	517	1.000	H→L (100%)	CAM-B3LYP	476	1.131	H→L (97%)
		407	0.409	H-1→L (97%)		354	0.549	H-1→L (87%)
		278	0.167	H→L+2 (96%)		249	0.135	H→L+1 (69%)
	PBE0	504	1.035	H→L (100%)	ω B97X-D	473	1.139	H→L (96%)
		393	0.435	H-1→L (97%)		349	0.560	H-1→L (89%)
		268	0.171	H→L+2 (94%)		250	0.132	H→L+1 (65%)
BG ⁺	PBE	578	0.917	H→L (100%)	M06	503	1.080	H→L (100%)
		468	0.308	H-1→L (95%)		393	0.456	H-1→L (97%)
		336	0.184	H→L+2 (96%)		270	0.151	H-1→L+2 (89%)
	BP86	577	0.918	H→L (100%)	M06-2X	493	1.210	H→L (96%)
		467	0.310	H-1→L (95%)		358	0.555	H-1→L (94%)
		336	0.184	H→L+2 (96%)		246	0.134	H→L+2 (46%) H→L+4 (32%)
	B3LYP	521	1.073	H→L (100%)	CAM-B3LYP	479	1.209	H→L (97%)

		407	0.422	H-1→L (97%)		353	0.563	H-1→L (92%)
		280	0.172	H→L+2 (94%)		251	0.124	H→L+1 (71%)
	PBE0	508	1.108	H→L (100%)	ωB97X-D	476	1.217	H→L (96%)
		392	0.450	H-1→L (95%)		348	0.577	H-1→L (89%)
		270	0.174	H→L+2 (96%)		252	0.123	H→L+1 (66%)
EG²⁺	PBE	595	0.776	H→L (100%)	M06	514	1.018	H→L (100%)
		464	0.294	H-1→L (94%)		380	0.423	H-1→L (96%)
		378	0.201	H→L+1 (21%) H→L+2 (76%)		299	0.148	H→L+1 (97%)
	BP86	594	0.779	H→L (100%)	M06-2X	501	1.144	H→L (98%)
		463	0.295	H-1→L (94%)		340	0.571	H-1→L (95%)
		378	0.198	H→L+1 (20%) H→L+2 (76%)		258	0.150	H→L+1 (84%)
	B3LYP	529	0.995	H→L (100%)	CAM-B3LYP	489	1.156	H→L (97%)
		393	0.394	H-1→L (96%)		335	0.568	H-1→L (94%)
		314	0.147	H→L+1 (87%)		250	0.163	H→L+1 (49%) H→L+2 (32%)
	PBE0	530	1.000	H→L (100%)	ωB97X-D	488	1.160	H→L (96%)
		393	0.446	H-1→L (97%)		331	0.591	H-1→L (89%)
		302	0.180	H→L+1 (98%)		245	0.167	H→L+1 (48%) H→L+2 (11%)

The predicted band positions for the three dyes are compared to the experimental spectra carried out in our laboratory or in the literature (See Figures S-1-S-3, Supplementary information). For the MG⁺ dye, the λ_{\max} calculated with eight functional cited in Table 3 are compared with the experimental spectrum carried out in our laboratory ($\lambda_{\max} = 615\text{nm}$, Figure S-1). The analysis of Table 1 shows that all the calculated λ_{\max} values are underestimated with respect to the experimental results. (The largest differences are respectively 139 nm and 142 nm for CAM-B3LYP and ω B97-XD). For the BG⁺ dye, the λ_{\max} calculated with eight functional are compared with the experimental results ($\lambda_{\max} = 625\text{nm}$, Figure S-2). Similarly, the analysis of Table 3 shows the underestimation of all the calculated λ_{\max} values (The largest differences are also 146 nm and 149 nm for CAM-B3LYP and ω B97X-D, respectively). For the EG²⁺ dye, the λ_{\max} calculated with eight functional are compared to the experimental results ($\lambda_{\max} = 632\text{nm}$, Figure S-3). The analysis of Table 3 shows that all the

calculated λ_{\max} values are underestimated compared to the experimental results. (The largest differences being 143 nm and 144 nm for CAM-B3LYP and ω B97X-D, respectively).

According to Table 1, it can be seen that the largest differences between calculated and experimental λ_{\max} wavelengths are those obtained with the range-separated functionals CAM-B3LYP and ω B97X-D. However, the best estimates for the three dyes are those obtained by the PBE functional with (experiment-theory) differences amounting 41, 47 and 37 nm for MG⁺, BG⁺, and EG²⁺ dyes, respectively. This feature is not to surprise, since it agrees with Jacquemin et al. conclusions in ref. [56] where the authors performed a critical assessment of the efficiency and consistency of range-separated hybrids for computing the main $\pi \rightarrow \pi^*$ transition of more than 100 organic dyes from the major classes of chromophores. Interestingly, it is important to emphasize that, whatever the functional is, all absorption wavelengths (λ_{\max}) correspond to HOMO to LUMO (H \rightarrow L) transitions, with contribution percentage of 96% ~100% within the eight functionals.

To see the influence of the solvation model on the displacements of the absorption wavelengths (λ_{\max}) and oscillator strength (f), as well as the orbitals involved in the transitions, the theoretical ultraviolet-visible absorption spectra of the three cationic dyes are calculated at two levels of theory (PBE and ω B97X-D) in SMD model solvation. Table 2 summarizes the results.

Comparing Table 1 with Table 2, it is clear that there is no significant effect of the solvation model on the absorption wavelengths (λ_{\max}), oscillator strength (f) and the orbitals involved in the transitions (only for ω B97X-D functional, the transition HOMO to LUMO+4 or LUMO+5 is observed)

An increase about 3-4 nm in absorption wavelengths (λ_{\max}) is observed using PBE functional. Whereas a displacement of 13 cm^{-1} towards large values is given by the ω B97X-D functional for both dyes MG^+ and BG^+ , the ω B97X-D gives almost the same wavelengths for EG^{2+} dyes, while the PBE give absorption wavelengths (λ_{\max}) less than around 5 nm with the CPCM model.

Table 2: Absorption wavelengths, oscillator strength (f), and the orbitals involved in the transitions of three dyes using two levels of theory. (SMD solvation model, nstates =20) H (HOMO), L (LUMO)

Dyes	Functionals	λ_{\max} (nm)	f	Transitions H=HOMO, L=LUMO (%)
MG^+	PBE	577	0.886	HOMO→LUMO (102%)
		467	0.285	HOM-1→LUMO (95%)
		340	0.184	HOMO→L+2 (96%)
	ω B97X-D	477	1.164	HOMO→LUMO (96%)
		347	0.554	HOM-1→LUMO (89%)
		243	0.099	HOMO→L+2 (21%), HOMO→L+4 (47%)
BG^+	PBE	582	0.941	HOMO→LUMO (102%)
		467	0.305	HOM-1→LUMO (95%)
		341	0.191	HOMO→L+2 (96%)
	ω B97X-D	489	1.207	HOMO→LUMO (96%)
		357	0.593	HOM-1→LUMO (90%)
		248	0.092	HOMO→L+2 (23%), HOMO→L+4 (45%)
EG^{2+}	PBE	590	0.816	HOMO→LUMO (101%)
		463	0.307	HOM-1→LUMO (94%)
		365	0.161	HOMO→L+2 (80%)
	ω B97X-D	487	1.156	HOMO→LUMO (96%)
		338	0.604	HOM-1→LUMO (90%)
		245	0.137	HOMO→L+1 (26%), HOMO→L+5 (40%)

All Absorption wavelengths can be characterized as $n \rightarrow \pi^*$ and $\pi \rightarrow \pi^*$ transitions type (related to the electronic transition of the π system of one phenyl ring and the lone pair of the nitrogen atoms as well as the π system of the phenyl rings and $\pi^* \text{C-N}$). Thus, these

transitions can be classically described as an intramolecular charge transfer (ICT) transition or local excitation (LE). Furthermore, as usual with this category of systems, there are other wavelengths with transitions involving different orbitals such as HOMO-1 \rightarrow LUMO, HOMO \rightarrow LUMO+1 or LUMO+2. Indeed, all eight functional produce three singlet excitations – local and charge-transfer.

From Fig.4 one sees that HOMO \rightarrow LUMO, LUMO+1 or LUMO+2 show a transfer towards the unsubstituted phenyl (MG⁺, BG⁺) or PhR3 (EG²⁺); these transitions can be classically described as an intramolecular charge transfer (ICT) transition. On the contrary, HOMO-1 exhibits localization similar to LUMO, so the transition HOMO-1 \rightarrow LUMO is more a local excitation (LE).

The excited states were examined with the Ciofini's charge transfer distance index, D_{CT} , which measures the spatial extent of charge transfer excitations and the charge passed Q_{CT} which is the integration of the density depletion function over all space.**[38]** The D_{CT} Indexes are calculated at four levels of theory in CPCM solvation model and are discussed in order to describe the nature of the CT states. Tables S-6-S-17 show the first ten excited states with their values of D_{CT} , Q_{CT} , and Excitation Energies. (See supporting information). Salient values are reported in Table 3, where we considered only the charge transfer excitations with sizable oscillator strength (*i.e.* the excitations mentioned in Table 1).

Table 3 : Excitation Energies in (eV), Distances between Donor and Acceptor groups ($d(N_D - N_A)$, in Å), Length, Charge and Dipole Moment (D_{CT} (Å), and Q_{CT} (a.u)) computed at different level of theory (PBE, PBE0, B3LYP and CAM-B3LYP/6-31G(d)/CPCM-H₂O). H (HOMO), L (LUMO)

Dyes	Functional	Excited State	Excitation Energies (eV)	$D(N_D-N_A)$ (Å)	D_{CT} (Å)	Q_{CT} (a.u)
MG ⁺	PBE	S ₁ H→L	2.19	5.112	2.556	0.688
		S ₂ H-1 → L	2.68	0.680	0.340	0.510
		S ₈ H→L+2	3.73	8.658	4.329	0.790
	PBE0	S ₁ H→L	2.45	4.148	2.074	0.654
		S ₂ H-1 → L	3.15	0.424	0.212	0.550
		S ₈ H→L+2	4.61	8.020	4.010	0.707
	B3LYP	S ₁ H→L	2.39	4.270	2.135	0.661
		S ₂ H-1 → L	3.04	0.488	0.244	0.551
		S ₈ H→L+2	4.44	8.316	4.158	0.742
	CAM-B3LYP	S ₁ H→L	2.56	3.408	1.704	0.637
		S ₂ H-1 → L	3.40	1.268	0.634	0.572
		S ₈ H→L+1	5.06	2.728	1.364	0.540
BG ⁺	PBE	S ₁ H→L	2.14	5.260	2.630	0.687
		S ₂ H-1 → L	2.64	0.852	0.426	0.507
		S ₈ H→L+2	3.68	8.632	4.316	0.778
	PBE0	S ₁ H→L	2.43	4.160	2.080	0.650
		S ₂ H-1 → L	3.15	0.472	0.236	0.546
		S ₈ H→L+2	4.59	7.862	3.931	0.692
	B3LYP	S ₁ H→L	2.37	4.284	2.142	0.657
		S ₂ H-1 → L	3.04	0.500	0.250	0.547
		S ₈ H→L+2	4.42	8.240	4.120	0.732
	CAM-B3LYP	S ₁ H→L	2.58	3.244	1.622	0.629
		S ₂ H-1 → L	3.50	1.434	0.717	0.570
		S ₈ H→L+1	5.09	2.540	1.270	0.541
EG2 ⁺	PBE	S ₁ H→L	2.08	6.160	3.080	0.693
		S ₂ H-1 → L	2.67	3.820	1.910	0.477
		S ₆ H→L+2	3.27	9.320	4.660	0.843
	PBE0	S ₁ H→L	2.33	4.540	2.270	0.645
		S ₂ H-1 → L	3.15	2.158	1.079	0.504
		S ₆ H→L+2	4.09	9.174	4.587	0.824
	B3LYP	S ₁ H→L	2.34	4.422	2.211	0.646
		S ₂ H-1 → L	3.15	1.980	0.990	0.498
		S ₆ H→L+2	3.94	8.562	4.281	0.720
	CAM-B3LYP	S ₁ H→L	2.53	3.070	1.535	0.612
		S ₂ H-1 → L	3.69	0.494	0.247	0.525
		S ₆ H→L+2	4.86	5.172	2.586	0.571

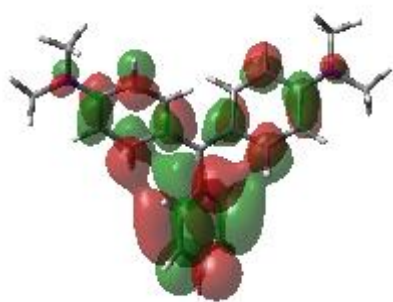
These excitations correspond to the first electronic transition ($S_1 \leftarrow S_0$) and to the second ($S_2 \leftarrow S_0$) for the three dyes. We studied also the eighth ES (i.e. $S_8 \leftarrow S_0$) for MG^+ , BG^+ and the sixth ES (i.e. $S_6 \leftarrow S_0$) for EG^{2+} , where in both cases these transitions correspond to a HOMO \rightarrow LUMO+2 excitation, as reported in Table 3. All the lowest lying charge transfer states correspond mainly to a one-electron excitation from HOMO to the LUMO (cf. Table 3).

For Q_{CT} (HOMO \rightarrow LUMO) the density analysis provides similar values for the two dyes MG^+ and BG^+ (variations between 0.001-0.008 (a.u.) with the four functionals PBE, PBE0, B3LYP and CAM-B3LYP respectively). For the EG^{2+} dye, the Q_{CT} calculated with the three functionals containing HF exchange (PBE0, B3LYP and CAM-B3LYP) is a bit smaller compared to the dyes MG^+ and BG^+ , whereas the PBE functional (GGA) gives a higher value. A ranking ($EG^{2+} < BG^+ < MG^+$) is observed. Consequently, the CT length (D_{CT}) associated to the first transition increases according to the $EG^{2+} > BG^+ > MG^+$ order and the range separated functionals give the smallest D_{CT} . The large values of D_{CT} are observed for the transitions HOMO \rightarrow LUMO, LUMO+1 or LUMO+2 (S_1 , S_6 , S_8) characterize an intramolecular charge transfer (ICT) transition. On the contrary, the small values of D_{CT} observed for the transition HOMO-1 \rightarrow LUMO (S_2) indicates a LE transition.

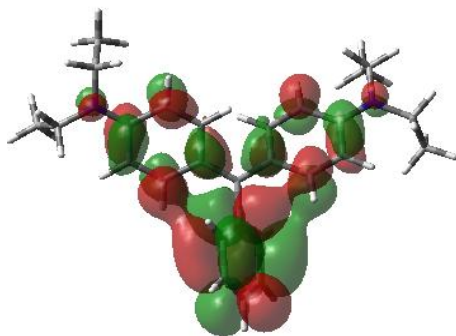
3.4. Energy levels of the molecular orbitals.

In relation to the absorption spectral analysis and the electron transitions between the orbitals, it is important to observe the HOMO, HOMO-1, LUMO, LUMO+1 and LUMO+2 which are the orbitals involved in such electron transitions, whose energy levels are shown in Figure S-4. As expected, the MO diagrams show increasing HOMO-LUMO gaps (hardness, as discussed above) between range-separated functionals and hybrids or GGA functionals.

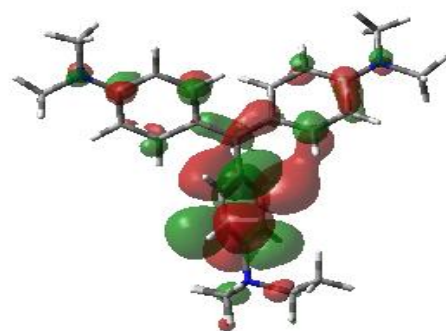
Mapping of HOMO and LUMO orbitals is important for observing charge separation; hence, it is obtained and analyzed as shown in Figure 4.



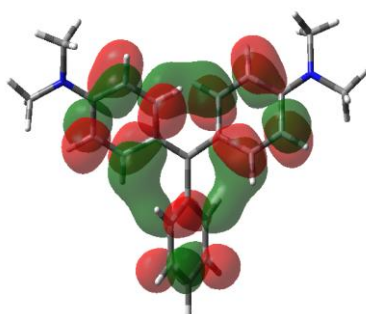
LUMO+2



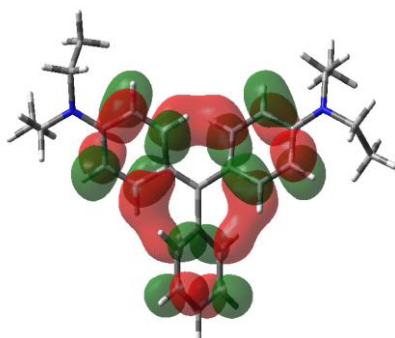
LUMO+2



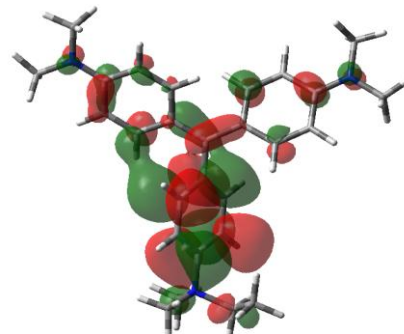
LUMO+2



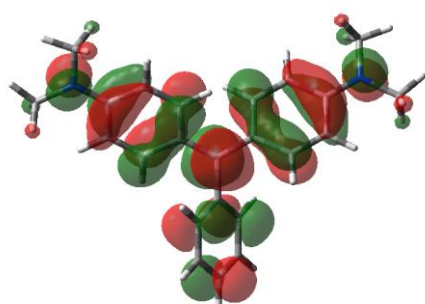
LUMO+1



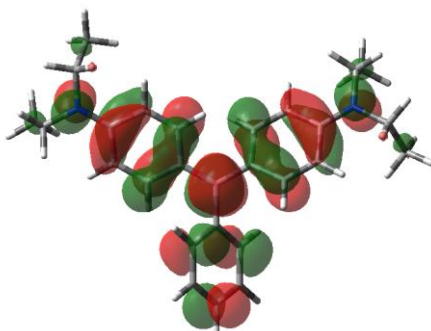
LUMO+1



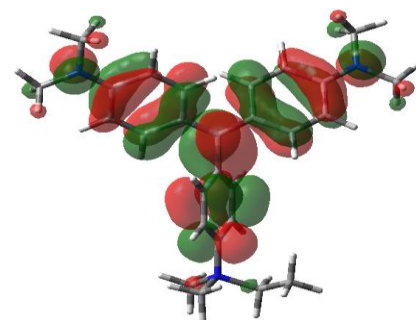
LUMO+1



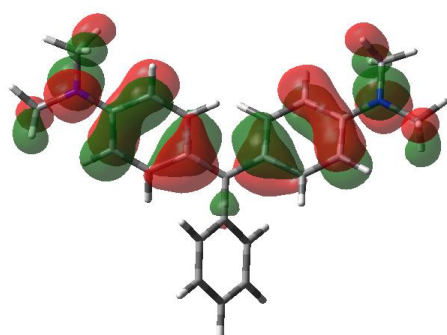
LUMO



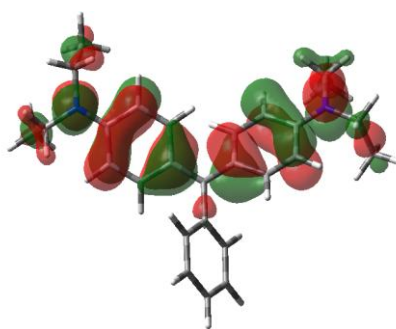
LUMO



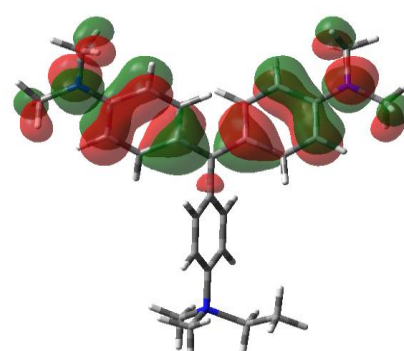
LUMO



HOMO



HOMO



HOMO

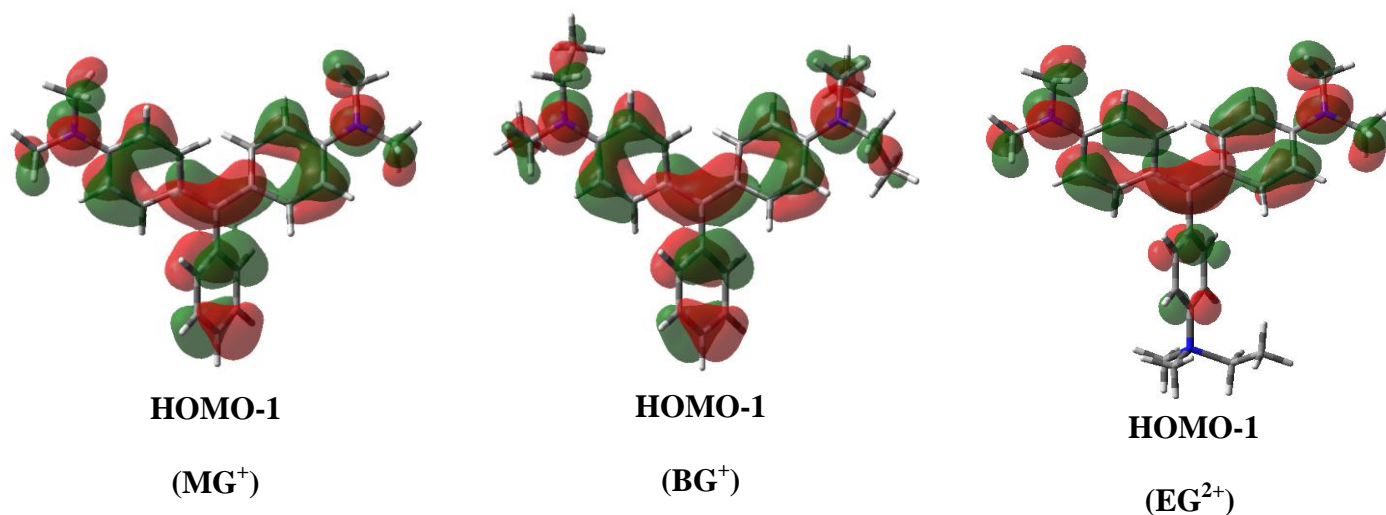


Figure 4. MO plots for three cationic dyes (B3LYP/6-31G(d) (isovalue 0.02))

Figure 4 shows the molecular orbitals (MOs) involved in the charge transfer (CT) transition in the three dyes. One can observe the similarities of HOMOs of the MG⁺, BG⁺ and EG²⁺ dyes, but with slight contribution differences. The study shows that the HOMO density is mostly concentrated in the two symmetric benzene rings and nitrogen atoms, while the LUMO density is more uniformly distributed over the three benzene rings which leads us to interpret that the three dyes have a high attractive capacity for electrons.[60]

3.5. Local reactivity descriptors.

Recently, Domingo et al. introduced the so-called local electrophilic, P_k^+ , and nucleophilic, P_k^- Parr functions, obtained from the Mulliken atomic spin density (ASD) at the radical cation and at the radical anion of the corresponding reagents.[61] The local, electrophilic and nucleophilic Parr functions P^\pm were defined from the similarity of the Electron Localization Function (ELF) proposed by Savin et al.[62,63] and the atomic spin densities $\rho_s^r \equiv \rho_\alpha^r - \rho_\beta^r$ of the radical anion (ra) of the electrophile A and the radical cation (rc) of the nucleophile B species.[61] The Parr functions, which are merely spin-polarized Fukui functions[64-66], were introduced simply to indicate that,

$$P_A^+ \equiv \rho_s(r)^{ra} \quad (1)$$

$$P_B^- \equiv \rho_s(r)^{rc} \quad (2)$$

P^+ will be associated to the local propensity of the electrophile (A) against a nucleophilic approach [61] and P^- will identify the local response of the nucleophile (B) against an electrophilic approach. The electrophilic P_k^+ , Parr functions are obtained by single-point energy calculations at the optimized neutral geometries using the unrestricted UB3LYP formalism and 6-31G (d) basis set. The calculated electrophilic Parr function for the three triphenylmethane dyes are reported in Figures 5-7.

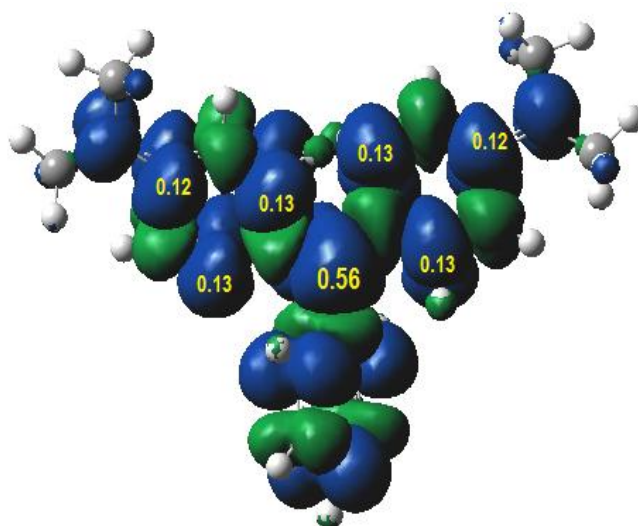


Figure 5: Map of ASD of MG^+ dye and the corresponding electrophilic Parr functions (isovalue 0.0004)

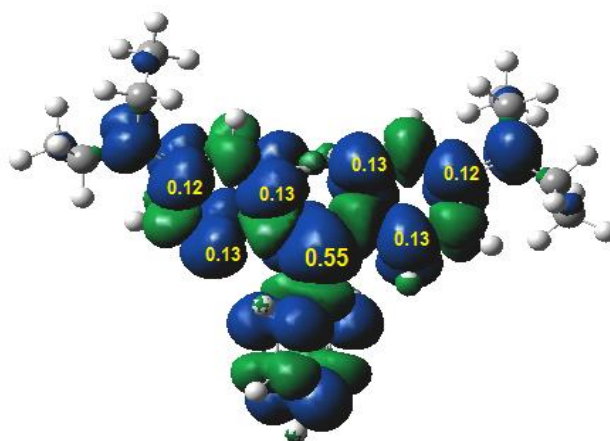


Figure 6: Map of ASD of BG^+ dye and the corresponding electrophilic Parr functions. (isovalue 0.0004)

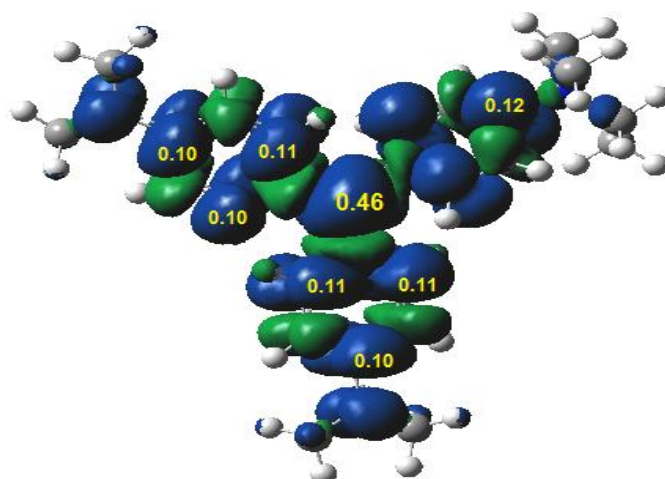


Figure 7: Map of ASD of EG^{2+} dye and the corresponding electrophilic Parr functions. (isovalue 0.0004)

Therefore, the C1 (central carbon) has the highest values (0.56, 0.55, 0.46). This result indicates that the C1 atom, the most electrophilic center of the three compounds will be the privileged site of attack (See Figures 5-7). These results are in agreement with the experimental results.

On the other hand, the reactivity–selectivity descriptor $\Delta f(\mathbf{r})$, introduced by Morell *et al.* [67,68] has been calculated. The descriptor $\Delta f(\mathbf{r})$, can be defined either as the response of the chemical hardness to external potential changes or the change of the Fukui function f at each point \mathbf{r} when the total number of electron is changed.

$$\Delta f(\mathbf{r}) = \left(\frac{\delta\eta}{\delta v(\mathbf{r})} \right)_N = \left(\frac{\partial f(\mathbf{r})}{\partial N} \right)_{v(\mathbf{r})} \quad (3)$$

Using finite difference approximations, the dual descriptor reads:

$$\Delta f(\mathbf{r}) \approx f^+(\mathbf{r}) - f^-(\mathbf{r}) \quad (4)$$

Where

$$f^+(\mathbf{r}) = \left(\frac{\Delta\mu^+}{\Delta v(\mathbf{r})} \right)_N = - \left(\frac{\Delta A}{\Delta v(\mathbf{r})} \right)_N \approx \rho^{LUMO}(\mathbf{r}) \quad (5)$$

$$f^-(\mathbf{r}) = \left(\frac{\Delta\mu^-}{\Delta v(\mathbf{r})} \right)_N = - \left(\frac{\Delta I}{\Delta v(\mathbf{r})} \right)_N \approx \rho^{HOMO}(\mathbf{r}) \quad (6)$$

Accordingly, when $\Delta f(\mathbf{r}) > 0$ then the point \mathbf{r} favours a nucleophilic attack, whereas if $\Delta f(\mathbf{r}) < 0$ then the point \mathbf{r} favors an electrophilic attack. Therefore, positive values of $\Delta f(\mathbf{r})$ identify electrophilic regions within the molecular topology, whereas negative values of $\Delta f(\mathbf{r})$ define nucleophilic regions. Thus, Figures 8-10 display a map of the nucleophilic/electrophilic behavior of the different sites within the molecule according to the $\Delta f(\mathbf{r})$ descriptor. The regions with $\Delta f(\mathbf{r}) > 0$ (yellow) where electrophilic regions are located in C1 (central carbon).

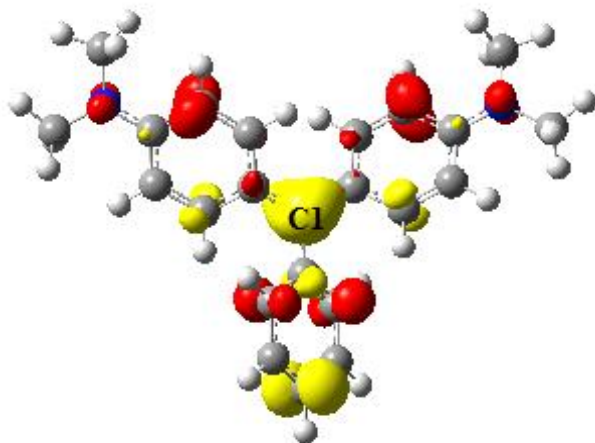


Figure 8. $\Delta f(r)$ of MG^+ dye calculated at the B3LYP/6-31G(d) level (isovalue 0.006)

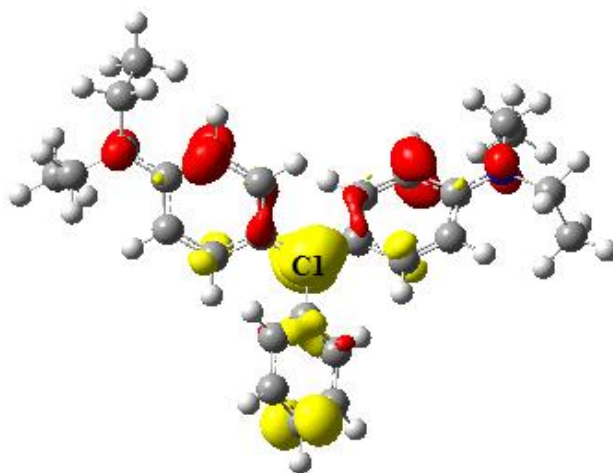


Figure 9. $\Delta f(r)$ of BG^+ dye calculated at the B3LYP/6-31G(d) level (isovalue 0.006)

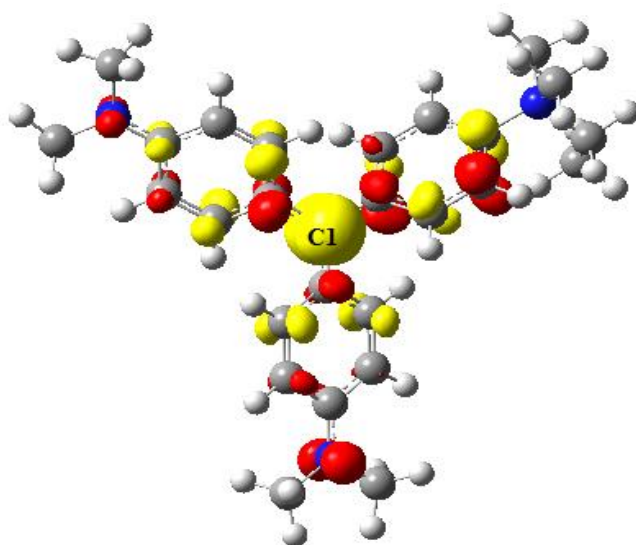
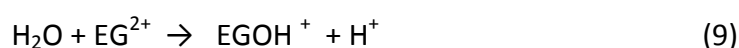
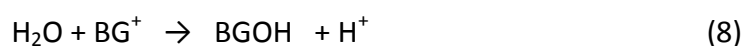
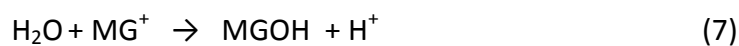


Figure 10. $\Delta f(r)$ of EG^{2+} dye calculated at the B3LYP/6-31G(d) level (isovalue 0.006)

3.6. Hydrolysis of dyes (decolorization)

Based on the cation structure of dyes, stabilized by the conjugation which delocalizes the positive charge, the hydrolysis mechanism should be a nucleophilic addition on a carbocation mechanism and the reaction rate is not related to the concentration of the nucleophile (H_2O) for the following reactions;



The reaction mechanisms of the three reactions has been studied at the B3LYP/6-31G* level of theory. Moreover, in all cases a unique transition state corresponding to the OH^- -C1 bond formation has been located and is depicted in Figure 11. The geometries of the products (MGOH, BGOH and $EGOH^+$) are schematically illustrated in Figure S-5.

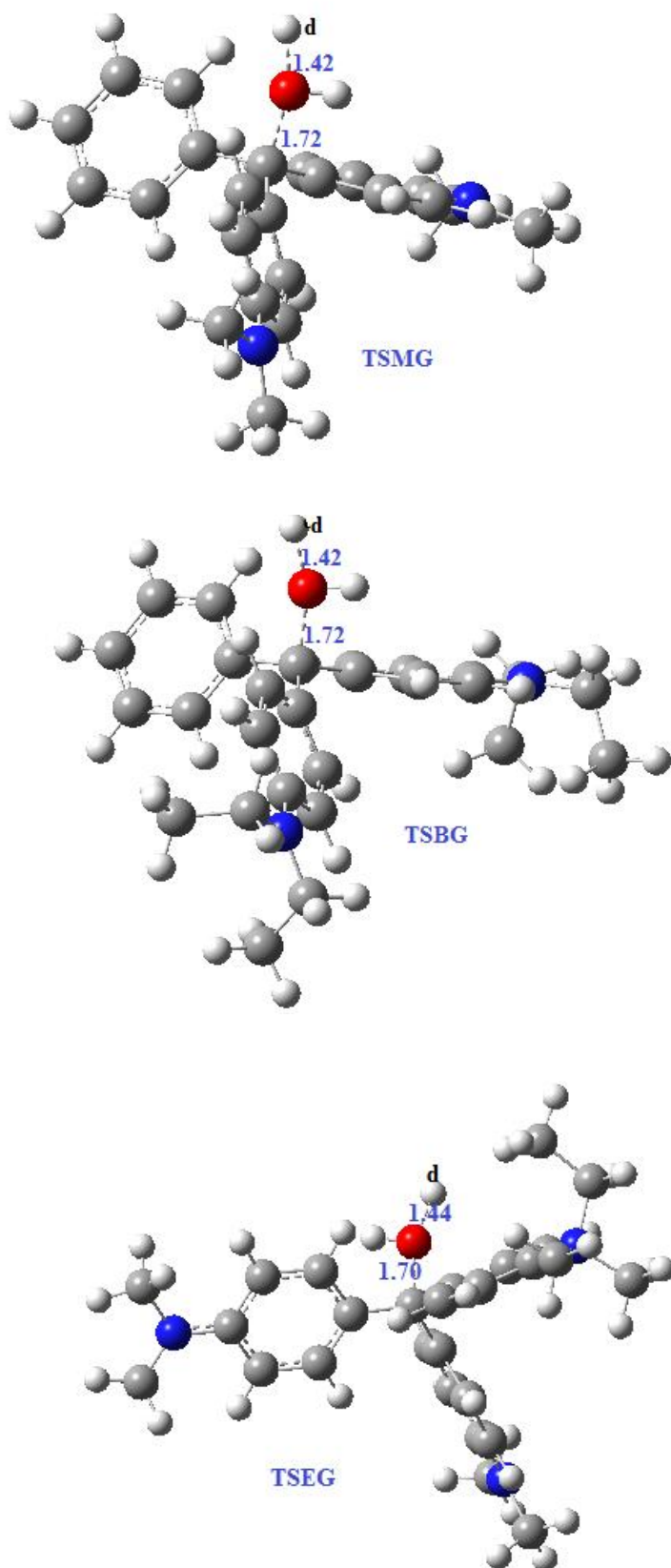


Figure 11. B3LYP/6-31G(d) optimized geometries for the transition structures for hydrolysis reactions. The distances C1-O and O-H_d detached are shown in Å.

If we monitor the distances of the bond formed and broken from reagents (MG^+ , BG^+ , EG^{2+} and H_2O) to the products (MGOH , BGOH and EGOH^+) (See Figure S-5) along with the TS structures (TSMG , TSGB and TSEG) (See Figure 11) it can be seen that: in the TSMG the distance $\text{C-O} = 1.72 \text{ \AA}$, therefore the oxygen approaches to C1 to make a bond, (distance C-O in the product is 1.45 \AA). The distance $\text{O-H}_d = 1.42 \text{ \AA}$, (Mulliken population of H_d is *ca* 0.0), the H^+ can be considered as detached (standard distance $\text{H-O} = 0.98 \text{ \AA}$). In the product MGOH , the distance C-O becomes 1.45 \AA and this is a standard distance for the C-O bond. The distance O-H_d becomes 2.82 \AA . In the TSBG the distance $\text{C-O} = 1.72 \text{ \AA}$, becomes 1.45 \AA in the BGOH product. The distance $\text{O-H}_d = 1.42 \text{ \AA}$ in TSBG becomes 2.81 \AA in product BGOH . For the TSEG the distance C-O (1.70 \AA) is a little shorter compared to TSMG or TSBG and become 1.44 \AA in product (EGOH^+), while the distance O-H_d ($= 1.44 \text{ \AA}$) in TSEG is a little longer compared to TSMG or TSBG .

Table 4 shows the thermodynamics parameters of the hydrolysis reaction for the three cation dyes calculated in gas phase at the B3LYP level of theory. All reactions are exothermic and the reaction (9) is more exothermic than the two other reactions. This is not to surprise since it involves a doubly charged cation. The reaction hydrolysis of these dyes are in the following order: $\text{BG}^+ < \text{MG}^+ < \text{EG}^{2+}$ (Table 4).

Table 4. Thermodynamics parameters (barriers (ΔE^\ddagger , kcal mol^{-1}), activation enthalpies (ΔH^\ddagger , kcal mol^{-1}) and Gibbs activation free energies (ΔG^\ddagger , kcal mol^{-1}) at 298.15 K of hydrolysis reaction, all calculations performed within gas phase at B3LYP/ 6-31G (d) level.

Dyes	ΔE	ΔH	ΔG	ΔE^\ddagger	ΔH^\ddagger	ΔG^\ddagger
MG^+	-61.04	-60.91	-54.64	46.50	47.15	38.13
BG^+	-59.55	-59.32	-53.23	45.10	45.64	53.23
EG^{2+}	-112.80	-112.66	-106.69	97.82	98.39	89.95

In the Table 5, the hydrolysis energies and barriers are reported as calculated at the eight levels of theory in gas phase medium.

Table 5. Thermodynamics parameters (barriers (ΔE^\ddagger , kcal mol⁻¹) at 298.15 K of hydrolysis reaction single point calculations at eight levels of theory (gas phase).

Functional	MG⁺		BG⁺		EG²⁺	
	ΔE	ΔE^\ddagger	ΔE	ΔE^\ddagger	ΔE	ΔE^\ddagger
PBE	-55.68	44.67	-53.64	42.85	-107.22	95.78
BP86	-52.57	44.71	-50.54	42.88	-103.93	96.68
B3LYP	-56.10	41.60	-54.35	40.00	-108.20	93.08
PBE0	-62.29	44.08	-60.34	42.37	-114.56	95.70
M06	-61.39	40.68	-59.00	38.48	-	93.14
M06-2X	-	47.73	-	45.80	-	99.39
CAM-B3LYP	-65.44	46.64	-63.80	45.11	-117.90	98.54
ωB97X-D	-65.93	44.09	-64.01	42.53	-118.74	95.23

One observes the same order of barriers ($BG^+ < MG^+ \ll EG^{2+}$). From Table 5 we can also see that the energy barriers for the MG^+ and BG^+ dyes increases in the following order: M06 < B3LYP < PBE0 < ω B97X-D < PBE < BP86 < CAM-B3LYP < M06-2X. Both GGA functionals (BP86 and PBE) give about the same barriers (44.67 kcal for MG^+ and 44.71 kcal for BG^+). For the EG^{2+} dye the energy barriers increases in a rather similar order: B3LYP < M06 < ω B97X-D < PBE0 < PBE \leq BP86 < CAM-B3LYP < M06-2X. For the three dyes, the functional M06-2X gives the greatest barriers and the M06 gives the lowest ones.

With the CPCM model of solvation, the barriers of these three reactions are calculated through single point calculations at the same level of theory. The results are collected in Table 6.

Table 6. Thermodynamics parameters (barriers (ΔE^\ddagger , kcal.mol⁻¹) at 298.15 K of hydrolysis reaction, CPCM single point calculations at eight levels of theory.

Functional	MG ⁺		BG ⁺		EG ²⁺	
	ΔE	ΔE^\ddagger	ΔE	ΔE^\ddagger	ΔE	ΔE^\ddagger
PBE	-26.81	16.77	-26.24	16.23	-30.62	19.94
BP86	-23.65	16.76	-23.09	16.21	-27.31	19.83
B3LYP	-26.83	12.41	-26.41	11.93	-30.79	15.98
PBE0	-33.69	16.07	-33.09	15.48	-41.00	23.03
M06	-32.33	12.15	-31.42	11.02	-	16.02
M06-2X	-	18.80	-	17.96	-	22.41
CAM-B3LYP	-36.23	17.59	-35.82	17.06	-40.02	21.35
ωB97X-D	-37.15	15.99	-36.47	15.41	-41.16	19.84

One can see that the energy barriers for the MG⁺ and BG⁺ dyes increase in the same order: M06 < B3LYP < ω B97X-D < PBE0 < BP86 < PBE < CAM-B3LYP < M06-2X and both GGA functionals (BP86 and PBE) give the same barriers. The M06-2X functional gives the greatest barriers and the M06 gives the lowest ones. One observes also the same order of barriers (BG⁺ < MG⁺ < EG²⁺) observed in gas phase. As expected, the barriers are strongly affected by taking into account the solvent medium, because the solvent (water) is polar and the dyes are positively charged (cations). More quantitatively, the significant shifts amount *ca* 28-34 kcal/mol for MG⁺ dyes, 27-33 kcal/mol for BG⁺ dyes, and 72-77 kcal/mol for EG²⁺ dyes, according to the functionals. These shifts have to be assigned to both of the electrostatic model used for approximating the solvation effect, (explaining the doubled shift found for EG²⁺ with respect to the monocations) and the need to consider water oligomers (dimer, trimer, ...) rather a single water molecule. The dependence of the solvation energy of cations with respect to the number of solvent molecules has been recently underlined for the proton solvation energy (see ref. [69-72] and ref. therein)

Within the SMD model of solvation [73], the barriers of the reactions (7) are calculated through geometry optimization calculations at four level of theory (PBE, BP86, B3LYP, PBE0) to see the impact of solvation models on energy barriers. In the four cases a unique transition state corresponding to the OH⁻-C1 bond formation has been located and is depicted in Figure S-6. The corresponding results of the thermodynamic parameters are gathered in Table 7. The latter shows barriers comparable to those found by the CPCM calculations at a single point (Table 8). Calculations for BG⁺ and EG2⁺ dyes did not converge.

Table 7. Thermodynamics parameters (barriers (ΔE^\ddagger , kcal mol⁻¹), activation enthalpies (ΔH^\ddagger , kcal mol⁻¹) and Gibbs activation free energies (ΔG^\ddagger , kcal mol⁻¹) at 298.15 K of MG⁺ hydrolysis reaction, after optimization with the SMD solvation model.

Functional	MG ⁺					
	ΔE	ΔH	ΔG	ΔE^\ddagger	ΔH^\ddagger	ΔG^\ddagger
PBE	-26.53	-26.92	-18.12	15.26	16.23	5.49
BP86	-	-	-	15.41	16.40	5.58
B3LYP	-25.35	-25.84	-16.73	10.70	11.85	0.49
PBE0	-32.88	-33.56	-24.25	13.95	15.06	3.94

More accurate calculations would need to perform calculations involving on the one hand explicit solvated proton, i.e. not only hydronium cation H₃O⁺ within the solvent model, but hydrated protons such as Zundel cation H⁺(H₂O)₂ [74], Eigen cation H₃O⁺(H₂O)₃ [74], Stoyanov cation H₅O₂⁺(H₂O)₄ [71], and, on the other hand, water dimer, tetramer or hexamer as reactants (to balance the hydrolysis equation). One of the major effect would be to get a better value for the solvated proton. This point is indeed a little more complex since the hydrogen bond between H₃O⁺ and one first neighbor H₂O has been calculated to amount *ca* 4.4 kcal/mol [76], to be compared to 2.5 kcal/mol in bulk water [77, 78]. According to the experimental technique used to tackle the dynamics of shell water molecules around ions, slower reorientation times than in the bulk are observed because of stronger hydrogen

bonds with H_3O^+ than in the bulk [79]. Nevertheless, four hydration shells have been assigned from Smiechowski and Stangret [80] in FTIR experiments. Besides, to be sufficiently accurate, the mechanism of water dissociation would involve a water cluster consisting in at least 6 water molecules, allowing a charge transfer through a proton shuttle mechanism process, allowing the unusually high diffusion rate. This mechanism is sometimes called "Grotthuss mechanism." [81-85] The solvation of the proton has been shown to involve both of the $\text{H}_3\text{O}^+(\text{H}_2\text{O})_3$ Eigen cation and the $\text{H}_3\text{O}^+(\text{H}_2\text{O})$ Zundel cation, i.e. $[\text{H}_2\text{O}-\text{H}-\text{OH}_2]^+$. Accordingly, whereas the thermodynamics resulting from our calculation dealing with a single proton H^+ solvated only by a continuum model cannot provide accurate values to be compared to experiment, the trends between the three triphenylmethane derivatives can be considered as trustable. One source of inaccuracy is certainly the solvation model, which leads to different results if one considers separate reactants –or products- (each one within its electrostatic model) or both reactants –or products- within a single solvent model. This is typically obtained if one considers the energies obtained from the sum of separate fragments, or the energy obtained at the feet of an IRC (intrinsic reaction path), followed by a subsequent geometry optimization of the resulting structures. Because of the existence of several degrees of freedom (rotations between conformers which can be overcome by thermal motion, the experimental data should lie between the theoretical (OK) values.

One should consider the obtained activation energies as minimal values (i.e. underestimate), because a) the solvation model, just discussed (the sum of the separate reactant energies is clearly higher than the energy of the gathered (weakly bonded) reactants; b) the DFT functionals selected in the present work may not be the best ones to calculate water proton-transfer reactions, as shown in [86]. One may also underline the well-known difficulty to

calculate proton-exchange barriers with DFT functionals [87, 88], as well as with more sophisticated methods.[89]

3.7. Ultraviolet-Visible spectra of the products.

For the three resulting products of equations (7)-(9) the λ_{\max} and the strength of the oscillator (f), as well as the orbitals involved in the transitions are calculated at the same seven levels of theory. Table 8 collects these results.

Table 8: Absorption wavelengths, oscillator strength (f), and the orbitals involved in the transitions of three products using eight levels of theory.

Product	Functionals	λ_{\max} (nm)	f	Transitions H=HOMO, L=LUMO (%)
MGOH	PBE	334	0.025	H-1 \rightarrow L+2 (76%)
	BP86	333	0.026	H-1 \rightarrow L+2 (76%)
	B3LYP	271	0.085	H \rightarrow L+1 (58%)
	PBE0	248	0.240	H \rightarrow L+3 (71%)
	M06	252	0.207	H \rightarrow L+3 (43%)
	M06-2X	237	0.924	H-1 \rightarrow L+3 (19%)
	CAM-B3LYP	237	0.877	H-1 \rightarrow L+3 (21%)
	ω B97X-D	236	0.907	H-1 \rightarrow L+3 (24%)
BGOH	PBE	339	0.022	H-1 \rightarrow L+2 (78%)
	BP86	338	0.022	H-1 \rightarrow L+2 (79%)
	B3LYP	257	0.609	H-1 \rightarrow L+3 (61%)
	PBE0	248	0.271	H-1 \rightarrow L+3 (50%)
	M06	255	0.210	H \rightarrow L+3 (54%)
	M06-2X	240	0.934	H-1 \rightarrow L+3 (19%)
	CAM-B3LYP	240	0.882	H-1 \rightarrow L+3 (21%)
	ω B97X-D	239	0.910	H-1 \rightarrow L+3 (24%)
EGOH ⁺	PBE	447	0.091	H \rightarrow L (85%)
	BP86	445	0.092	H \rightarrow L (85%)
	B3LYP	249	0.736	H-1 \rightarrow L+3 (85%)
	PBE0	245	0.480	H-1 \rightarrow L+3 (41%)
	M06	251	0.624	H-1 \rightarrow L+3 (59%)
	M06-2X	236	0.743	H-1 \rightarrow L+3 (77%)
	CAM-B3LYP	237	0.710	H-1 \rightarrow L+3 (82%)
	ω B97X-D	236	0.685	H-1 \rightarrow L+3 (82%)

As expected, all the main bands appear in the UV region (200-400 nm), corresponding to the extinction of the colored bands of the dyes. It is noticeable that the transition energy is calculated with GGA functionals at smaller energies (larger wavelength) than with hybrid and even more with range-separated functionals. This is in agreement with the larger gap (hardness) obtained by hybrid and range-separated functionals with respect to GGAs. In case of EGOH⁺ product, the GGA functional gives the bands in the purple region. For all products, the absorption wavelengths systematically obey the trend: PBE > BP86 > B3LYP > M06 > PBE0 > M06-2X = CAM-B3LYP > ω B97X-D, so more generally GGA > hybrid > range-separated classes of functional. This underlines the (well-known) importance of the asymptotic behavior of the Kohn-Sham potential for the calculation of electronic spectra. The fact that the PBE functional delivers the best agreement with experimental absorption spectra is probably related to the solvent model interaction with charged species, whereas no significant effect has been found with respect to the basis set.

4. Concluding remarks

In the present work, the degradation of three triphenylmethane dyes (MG⁺, BG⁺, EG²⁺) is studied at DFT and TD-DFT levels. As expected, the geometry optimizations of the dyes recovers the planarity of the ring group of the triphenylmethane and the DFT reactivity descriptors show that the EG²⁺ dye is more reactive than MG⁺ and BG⁺ dyes. The UV/vis spectra of three dyes are well reproduced using TDDFT method. The agreements with the experimentally observed wavelength values obey the trend: PBE > BP86 > B3LYP > PBE0 > M06 > M06-2X > CAM-B3LYP > ω B97X-D. The range-separated functionals lead to larger differences between calculated λ_{max} quantities and experimental results. The two Local

reactivity descriptors used in this work show that the C1 (central carbon) is the most active site involved in the degradation process.

The degradation of the triphenylmethane dyes through a hydrolysis mechanism is found exothermic. The barriers are in order: $BG^+ < MG^+ < EG^{2+}$ in gas and solution phase. In the two phases CAM-B3LYP functional gives the greatest barriers and the M06 gives the lowest ones. These barrier ranges are compatible to a slow degradation through hydrolysis. Ultraviolet-visible spectra of the products appear in the UV region (200-400 nm) and the absorption wavelengths systematically obey the trend $GGA > \text{hybrid} > \text{range-separated}$ classes of functionals.

Author Contributions

Conceptualization and methodology: D.T, N.L, and H.C; Investigation: D.T, N.L, and H.C; Writing – Original Draft Preparation: N.L and H.C; Writing – Review & Editing : C.M, L.M, N.L.,H.C.; Experimental measurements: D.T, N.L, H.M, B.W; Resources : N.M, N.O, C.M; Data Curation: D.T, N.L, L.M, and H.C. All authors have read and agreed to the published version of the manuscript.

Acknowledgements

N.L. acknowledges the financial support of the Algerian Ministry of Higher Education and Scientific Research and the DGRSDT (Research Project B00L01UN280120220002). The GENCI/CINES (Project cpt2130) and the PSMN of the ENS-Lyon are acknowledged for HPC resources/computer time.

This research did not receive any specific grant from funding agencies in the public, commercial, or not-for-profit sectors.

ORCID:

Nadjia Latelli: nadjia.latelli@univ-msila.dz ORCID 0000-0002-6206-9228
 Hafida Merouani: h.merouani@univ-batna2.dz ORCID 0000-0003-1387-3049
 Nadia Ouddai : nadia.ouddai@univ-batna.dz ORCID 0000-0002-9083-5559
 Henry Chermette: henry.chermette@univ-lyon1.fr, ORCID 0000-0002-5890-7479
 Christophe Morell: Christophe.Morell@univ-lyon1.fr, ORCID 0000-0002-6321-8723
 Lynda Merzoud: lyndamerzoud@gmail.com ORCID 0000-0002-6003-8882
 Naima Mechehoud naima.mechehoud@univ-batna.dz

Appendix A. Supplementary information

Supplementary information related to this article can be found at <http://.....>

Table S-1: Selected bond lengths and angles (gas phase) of three dyes calculated by eight functional

Table S-2: MPA atomic charges of three dyes calculated by eight functionals

Table S-3: NPA atomic charges of three dyes calculated by eight functionals

Figure S-1: Experimental UV-Visible spectra of MG dye at pH=7.80, [MG]₀=7mg/l

Figure S-2: Experimental UV-Visible spectra of BG dye (7 mg/l)

Figure S-3: Experimental UV-Visible spectra of EG dye (11mg/l)

Table S-4: Quantum chemical descriptors of three cationic dyes in gas phase calculated at eight levels of theory

Table S-5: Quantum chemical descriptors of three cationic dyes in aqueous phase (single points, CPCM model) calculated at eight levels of theory. The origin of the coordinates is taken at the center of mass.

Tables S-6—S-17: DCT charge transfer diagnostic using the unrelaxed electronic density difference (6-31G (d), CPCM, water):

MG dye: Table S-4: PBE; Table S-5: PBE0; Table S-6: B3LYP; Table S-7: CAM-B3LYP

BG dye: Table S-8: PBE; Table S-9: PBE0; Table S-10: B3LYP; Table S-11: CAM-B3LYP

EG dye: Table S-12: PBE; Table S-13: PBE0; Table S-14: B3LYP; Table S-15: CAM-B3LYP

Figure S-4: Orbital energy levels of three cationic dyes at eight levels of calculation

Figure S-5. B3LYP/6-31G(d) optimized geometries of the products for hydrolysis reactions. The distances C1-O and O-H_d detached are shown in Å.

Figure S-6. Optimized geometries for the transition structures for hydrolysis reactions.

Cartesian coordinates of the optimized structures of the three dyes MG⁺, BG⁺ and EG²⁺ calculated with eight functional (PBE, BP86, B3LYP, PBE0, M06, CAM-B3LYP, WB97X-D and M06-2X) and 6-31G (d) basis.

References:

- [1] C. W. Looney and W. T. Simpson, "Structures and π -Electron Spectra. III. Triphenylmethane Dyes 1, 2, 3," *J. Am. Chem. Soc.*, vol. 76, no. 24, pp. 6293–6300, 1954.
- [2] S. Bendjabeur, R. Zouaghi, B. Zouhoune, and T. Sehili, "DFT and TD-DFT insights, photolysis and photocatalysis investigation of three dyes with similar structure under UV irradiation with and without TiO₂ as a catalyst: Effect of adsorption, pH and light intensity," *Spectrochim. Acta Part A Mol. Biomol. Spectrosc.*, vol. 190, pp. 494–505, 2018.
- [3] R. Soto-Rojo, J. Baldenebro-López, and D. Glossman-Mitnik, "Study of chemical reactivity in relation to experimental parameters of efficiency in coumarin derivatives for dye sensitized solar cells using DFT," *Phys. Chem. Chem. Phys.*, vol. 17, no. 21, pp. 14122–14129, 2015.
- [4] C. C. Barker, M. H. Bride, G. Hallas, and A. Stamp, "249. Steric effects in di- and tri-arylmethanes. Part III. Electronic absorption spectra of derivatives of Malachite Green containing substituents in the phenyl ring," *J. Chem. Soc.*, pp. 1285–1290, 1961.
- [5] R. A. Engh, J. W. Petrich, and G. R. Fleming, "Removal of coherent coupling artifact in ground-state recovery experiments: malachite green in water-methanol mixtures," *J. Phys. Chem.*, vol. 89, no. 4, pp. 618–621, 1985.
- [6] T. Lian, B. Locke, Y. Kholodenko, and R. M. Hochstrasser, "Energy flow from solute to solvent probed by femtosecond IR spectroscopy: malachite green and heme protein solutions," *J. Phys. Chem.*, vol. 98, no. 45, pp. 11648–11656, 1994.
- [7] Y. Nagasawa, Y. Ando, and T. Okada, "Solvent dependence of ultrafast ground state recovery of the triphenylmethane dyes, brilliant green and malachite green," *Chem. Phys. Lett.*, vol. 312, no. 2–4, pp. 161–168, 1999.
- [8] R. Miyata, Y. Kimura, and M. Terazima, "Intermolecular energy transfer from the photo-excited molecule to solvent: Malachite Green," *Chem. Phys. Lett.*, vol. 365, no. 5–6, pp. 406–412, 2002.
- [9] P. Sen, S. Yamaguchi, and T. Tahara, "Ultrafast dynamics of malachite green at the air/water interface studied by femtosecond time-resolved electronic sum frequency generation (TR-ESFG): an indicator for local viscosity," *Faraday Discuss.*, vol. 145, pp. 411–428, 2010.
- [10] G. Li, D. Magana, and R. B. Dyer, "Direct observation and control of ultrafast photoinduced twisted intramolecular charge transfer (TICT) in triphenyl-methane dyes," *J. Phys. Chem. B*, vol. 116, no. 41, pp. 12590–12596, 2012.
- [11] J. Yang, X. Yang, Y. Lin, T. B. Ng, J. Lin, and X. Ye, "Laccase-catalyzed decolorization of malachite green: performance optimization and degradation mechanism," *PLoS One*, vol. 10, no. 5, p. e0127714, 2015.
- [12] J. Wang *et al.*, "Pathway and molecular mechanisms for malachite green biodegradation in *Exiguobacterium* sp. MG2," *PLoS One*, vol. 7, no. 12, p. e51808, 2012.
- [13] P. Navarro, J. P. Zapata, G. Gotor, R. Gonzalez-Olmos, and V. M. Gómez-López,

- “Degradation of malachite green by a pulsed light/H₂O₂ process,” *Water Sci. Technol.*, vol. 79, no. 2, pp. 260–269, 2019.
- [14] D. Guillaumont and S. Nakamura, “Calculation of the absorption wavelength of dyes using time-dependent density-functional theory (TD-DFT),” *Dye. Pigment.*, vol. 46, no. 2, pp. 85–92, 2000.
- [15] J. Preat, D. Jacquemin, V. Wathélet, J.-M. André, and E. A. Perpète, “Towards the understanding of the chromatic behaviour of triphenylmethane derivatives,” *Chem. Phys.*, vol. 335, no. 2–3, pp. 177–186, 2007.
- [16] S. Rafiq, R. Yadav, and P. Sen, “Microviscosity inside a nanocavity: a femtosecond fluorescence up-conversion study of malachite green,” *J. Phys. Chem. B*, vol. 114, no. 44, pp. 13988–13994, 2010.
- [17] A. Nakayama and T. Taketsugu, “Ultrafast nonradiative decay of electronically excited states of malachite green: Ab initio calculations,” *J. Phys. Chem. A*, vol. 115, no. 32, pp. 8808–8815, 2011.
- [18] B.-B. Xie, S.-H. Xia, L.-H. Liu, and G. Cui, “Surface-hopping dynamics simulations of malachite green: a triphenylmethane dye,” *J. Phys. Chem. A*, vol. 119, no. 22, pp. 5607–5617, 2015.
- [21] M. J. Frisch, “Gaussian 09, version A. 1,” *Gaussian Inc., Pittsburgh, PA, USA*, 2009.
- [22] J. P. Perdew, K. Burke, and M. Ernzerhof, “Generalized gradient approximation made simple,” *Phys. Rev. Lett.*, vol. 77, no. 18, p. 3865, 1996.
- [23] J. P. Perdew, “Density-functional approximation for the correlation energy of the inhomogeneous electron gas,” *Phys. Rev. B*, vol. 33, no. 12, p. 8822, 1986.
- [24] A. D. Becke, “Density-functional exchange-energy approximation with correct asymptotic behavior,” *Phys. Rev. A*, vol. 38, no. 6, p. 3098, 1988.
- [25] S. H. Vosko, L. Wilk, and M. Nusair, “Accurate spin-dependent electron liquid correlation energies for local spin density calculations: a critical analysis,” *Can. J. Phys.*, vol. 58, no. 8, pp. 1200–1211, 1980.
- [26] A. D. Becke, “Density-Functional Thermochemistry. III. The Role of Exact Exchange. *J. Chem. Phys.*, 98: 5648-5652.” 1993.
- [27] Y. Zhao and D. G. Truhlar, “The M06 suite of density functionals for main group thermochemistry, thermochemical kinetics, noncovalent interactions, excited states, and transition elements: two new functionals and systematic testing of four M06-class functionals and 12 other function,” *Theor. Chem. Acc.*, vol. 120, no. 1, pp. 215–241, 2008.
- [28] Y. Zhao, N. E. Schultz, and D. G. Truhlar, “Design of density functionals by combining the method of constraint satisfaction with parametrization for thermochemistry, thermochemical kinetics, and noncovalent interactions,” *J. Chem. Theory Comput.*, vol. 2, no. 2, pp. 364–382, 2006.
- [29] C. Adamo and V. Barone, “Toward reliable density functional methods without adjustable parameters: The PBE0 model,” *J. Chem. Phys.*, vol. 110, no. 13, pp. 6158–6170, 1999.

- [30] T. Yanai, D. P. Tew, and N. C. Handy, "A new hybrid exchange–correlation functional using the Coulomb-attenuating method (CAM-B3LYP)," *Chem. Phys. Lett.*, vol. 393, no. 1–3, pp. 51–57, 2004.
- [31] J.-D. Chai and M. Head-Gordon, "Systematic optimization of long-range corrected hybrid density functionals," *J. Chem. Phys.*, vol. 128, no. 8, p. 84106, 2008.
- [32] W. J. Hehre, R. Ditchfield, and J. A. Pople, "Self-consistent molecular orbital methods. XII. Further extensions of Gaussian-type basis sets for use in molecular orbital studies of organic molecules," *J. Chem. Phys.*, vol. 56, no. 5, pp. 2257–2261, 1972.
- [33] M. Cossi, N. Rega, G. Scalmani, and V. Barone, "Energies, structures, and electronic properties of molecules in solution with the C-PCM solvation model," *J. Comput. Chem.*, vol. 24, no. 6, pp. 669–681, 2003.
- [34] V. Barone and M. Cossi, "Quantum calculation of molecular energies and energy gradients in solution by a conductor solvent model," *J. Phys. Chem. A*, vol. 102, no. 11, pp. 1995–2001, 1998.
- [35] R. Improta, "Uv-visible absorption and emission energies in condensed phase by PCM/TD-DFT methods," *Comput. Strateg. Spectrosc. from small Mol. to Nanosyst. Wiley, Chichester*, pp. 39–76, 2012.
- [36] S. Kawauchi, L. Antonov, and Y. Okuno, "Prediction of the color of dyes by using time-dependent density functional theory (TD-DFT)," *Bulg. Chem. Commun*, vol. 46, pp. 228–237, 2014.
- [37] M. J. Frisch *et al.*, "Gaussian 16 revision a. 03. 2016; gaussian inc," *Wallingford CT*, vol. 2, no. 4, 2016.
- [38] T. Le Bahers, C. Adamo, and I. Ciofini, "A qualitative index of spatial extent in charge-transfer excitations," *J. Chem. Theory Comput.*, vol. 7, no. 8, pp. 2498–2506, 2011.
- [39] F. Weinhold and C. R. Landis, *Valency and bonding: a natural bond orbital donor-acceptor perspective*. Cambridge University Press, 2005.
- [40] P. Andersen, "An electron diffraction investigation of triphenylmethane in gas phase," *ACTA Chem. Scand.*, vol. 19, no. 3, p. 622, 1965.
- [41] P. Andersen and B. Klewe, "The Crystal Structure of the Free Radical Tri-p-nitrophenylmethyl," *Acta Chem. Scand*, vol. 21, no. 10, p. 2, 1967.
- [42] D. G. Lister, J. K. Tyler, J. H. Høg, and N. W. Larsen, "The microwave spectrum, structure and dipole moment of aniline," *J. Mol. Struct.*, vol. 23, no. 2, pp. 253–264, 1974.
- [43] M. Fukuyo, K. Hirotsu, and T. Higuchi, "The structure of aniline at 252 K," *Acta Crystallogr. Sect. B Struct. Crystallogr. Cryst. Chem.*, vol. 38, no. 2, pp. 640–643, 1982.
- [44] J. Kreutzer, P. Blaha, and U. Schubert, "Assessment of different basis sets and DFT functionals for the calculation of structural parameters, vibrational modes and ligand binding energies of Zr4O2 (carboxylate) 12 clusters," *Comput. Theor. Chem.*, vol. 1084, pp. 162–168, 2016.
- [45] H. Chermette, "Chemical reactivity indexes in density functional theory," *J. Comput.*

- Chem.*, vol. 20, no. 1, pp. 129–154, 1999.
- [46] R. G. Parr and R. G. Pearson, "Absolute hardness: companion parameter to absolute electronegativity," *J. Am. Chem. Soc.*, vol. 105, no. 26, pp. 7512–7516, 1983.
- [47] J. Martínez, "Local reactivity descriptors from degenerate frontier molecular orbitals," *Chem. Phys. Lett.*, vol. 478, no. 4–6, pp. 310–322, 2009.
- [48] R. El Haouti *et al.*, "Cationic dyes adsorption by Na-Montmorillonite Nano Clay: Experimental study combined with a theoretical investigation using DFT-based descriptors and molecular dynamics simulations," *J. Mol. Liq.*, vol. 290, p. 111139, 2019.
- [49] D. Jacquemin, X. Assfeld, J. Preat, and E. A. Perpète, "Comparison of theoretical approaches for predicting the UV/Vis spectra of anthraquinones," *Mol. Phys.*, vol. 105, no. 2–3, pp. 325–331, 2007.
- [50] E. A. Perpète, C. Lambert, V. Wathélet, J. Preat, and D. Jacquemin, "Ab initio studies of the λ_{max} of naphthoquinones dyes," *Spectrochim. Acta Part A Mol. Biomol. Spectrosc.*, vol. 68, no. 5, pp. 1326–1333, 2007.
- [51] D. Jacquemin, J. Preat, V. Wathélet, M. Fontaine, and E. A. Perpète, "Thioindigo dyes: highly accurate visible spectra with TD-DFT," *J. Am. Chem. Soc.*, vol. 128, no. 6, pp. 2072–2083, 2006.
- [52] D. Jacquemin, J. Preat, V. Wathélet, and E. A. Perpète, "Substitution and chemical environment effects on the absorption spectrum of indigo," *J. Chem. Phys.*, vol. 124, no. 7, p. 74104, 2006.
- [53] E. A. Perpète, J. Preat, J.-M. André, and D. Jacquemin, "An ab initio study of the absorption spectra of indirubin, isoindigo, and related derivatives," *J. Phys. Chem. A*, vol. 110, no. 17, pp. 5629–5635, 2006.
- [54] D. Jacquemin *et al.*, "Time-dependent density functional theory investigation of the absorption, fluorescence, and phosphorescence spectra of solvated coumarins," *J. Chem. Phys.*, vol. 125, no. 16, p. 164324, 2006.
- [55] E. A. Perpète, F. Maurel, and D. Jacquemin, "TD- DFT Investigation of Diarylethene Dyes with Cyclopentene, Dihydrothiophene, and Dihydropyrrole Bridges," *J. Phys. Chem. A*, vol. 111, no. 25, pp. 5528–5535, 2007.
- [56] D. Jacquemin, E. A. Perpète, G. E. Scuseria, I. Ciofini, and C. Adamo, "TD-DFT performance for the visible absorption spectra of organic dyes: conventional versus long-range hybrids," *J. Chem. Theory Comput.*, vol. 4, no. 1, pp. 123–135, 2008.
- [57] D. Jacquemin, E. A. Perpète, G. Scalmani, M. J. Frisch, R. Kobayashi, and C. Adamo, "Assessment of the efficiency of long-range corrected functionals for some properties of large compounds," *J. Chem. Phys.*, vol. 126, no. 14, p. 144105, 2007.
- [58] D. Jacquemin, J. Preat, M. Charlot, V. Wathélet, J.-M. André, and E. A. Perpète, "Theoretical investigation of substituted anthraquinone dyes," *J. Chem. Phys.*, vol. 121, no. 4, pp. 1736–1743, 2004.
- [59] E. A. Perpète, V. Wathélet, J. Preat, C. Lambert, and D. Jacquemin, "Toward a theoretical quantitative estimation of the λ_{max} of anthraquinones-based dyes," *J.*

- Chem. Theory Comput.*, vol. 2, no. 2, pp. 434–440, 2006.
- [60] A. El Kassimi, A. Boutouil, M. El Himri, M. R. Laamari, and M. El Haddad, “Selective and competitive removal of three basic dyes from single, binary and ternary systems in aqueous solutions: A combined experimental and theoretical study,” *J. Saudi Chem. Soc.*, vol. 24, no. 7, pp. 527–544, 2020.
- [61] L. R. Domingo, P. Pérez, and J. A. Sáez, “Understanding the local reactivity in polar organic reactions through electrophilic and nucleophilic Parr functions,” *RSC Adv.*, vol. 3, no. 5, pp. 1486–1494, 2013.
- [62] A. Savin, B. Silvi, and F. Colonna, “Topological analysis of the electron localization function applied to delocalized bonds,” *Can. J. Chem.*, vol. 74, no. 6, pp. 1088–1096, 1996.
- [63] A. Savin, R. Nesper, S. Wengert, and T. F. Fässler, “ELF: The electron localization function,” *Angew. Chemie Int. Ed. English*, vol. 36, no. 17, pp. 1808–1832, 1997.
- [64] E. Chamorro, P. Pérez, and L. R. Domingo, “On the nature of Parr functions to predict the most reactive sites along organic polar reactions,” *Chem. Phys. Lett.*, vol. 582, pp. 141–143, 2013, doi: 10.1016/j.cplett.2013.07.020.
- [65] E. Chamorro and P. Pérez, “Condensed-to-atoms electronic Fukui functions within the framework of spin-polarized density-functional theory,” *J. Chem. Phys.*, vol. 123, no. 11, p. 114107, 2005.
- [66] M. Galván, A. Vela, and J. L. Gázquez, “Chemical reactivity in spin-polarized density functional theory,” *J. Phys. Chem.*, vol. 92, no. 22, pp. 6470–6474, 1988, doi: 10.1021/j100333a056.
- [67] C. Morell, A. Grand, and A. Toro-Labbe, “New dual descriptor for chemical reactivity,” *J. Phys. Chem. A*, vol. 109, no. 1, pp. 205–212, 2005.
- [68] C. Morell, A. Grand, and A. Toro-Labbé, “Theoretical support for using the $\Delta f(r)$ descriptor,” *Chem. Phys. Lett.*, vol. 425, no. 4–6, pp. 342–346, 2006.
- [69] H. Abdoul-Carime *et al.*, “Velocity of a Molecule Evaporated from a Water Nanodroplet: Maxwell-Boltzmann Statistics versus Non-Ergodic Events (Angew. Chem. Int. Ed. 54, 14685-14689),” *Angew. Chem. Int. Ed.*, 2014.
- [70] F. Mechacht, S. Lakehal, A. Lakehal, C. Morell, L. Merzoud, and H. Chermette, “Predicted structure and selectivity of 3d transition metal complexes with glutamic N, N-bis (carboxymethyl) acid,” *New J. Chem.*, vol. 45, no. 39, pp. 18366–18378, 2021.
- [71] E. S. Stoyanov, I. V Stoyanova, and C. A. Reed, “The structure of the hydrogen ion (H₃O⁺) in water,” *J. Am. Chem. Soc.*, vol. 132, no. 5, pp. 1484–1485, 2010.
- [72] F. Berthias *et al.*, “Proton migration in clusters consisting of protonated pyridine solvated by water molecules,” *ChemPhysChem*, vol. 16, no. 15, pp. 3151–3155, 2015.
- [73] A. V Marenich, C. J. Cramer, and D. G. Truhlar, “Universal solvation model based on solute electron density and on a continuum model of the solvent defined by the bulk dielectric constant and atomic surface tensions,” *J. Phys. Chem. B*, vol. 113, no. 18, pp. 6378–6396, 2009.

- [74] P. Schuster, "In The Hydrogen Bond, vol. II, Schuster P, Zundel G, Sandorfy C." North-Holland: Amsterdam, 1976.
- [75] M. Eigen, "Proton transfer, acid-base catalysis, and enzymatic hydrolysis. Part I: elementary processes," *Angew. Chemie Int. Ed. English*, vol. 3, no. 1, pp. 1–19, 1964.
- [76] N. Agmon, "Hydrogen bonds, water rotation and proton mobility," *J. Chim. Phys. Phys. Chim. Biol.*, vol. 93, pp. 1714–1736, 1996.
- [77] G. E. Walrafen, M. R. Fisher, M. S. Hokmabadi, and W. Yang, "Temperature dependence of the low-and high-frequency Raman scattering from liquid water," *J. Chem. Phys.*, vol. 85, no. 12, pp. 6970–6982, 1986.
- [78] D. M. Carey and G. M. Korenowski, "Measurement of the Raman spectrum of liquid water," *J. Chem. Phys.*, vol. 108, no. 7, pp. 2669–2675, 1998.
- [79] C. A. Reed, "Myths about the proton. The nature of H⁺ in condensed media," *Acc. Chem. Res.*, vol. 46, no. 11, pp. 2567–2575, 2013.
- [80] M. Śmiechowski and J. Stangret, "Proton hydration in aqueous solution: Fourier transform infrared studies of HDO spectra," *J. Chem. Phys.*, vol. 125, no. 20, p. 204508, 2006.
- [81] D. C. Rees and W. N. Lipscomb, "Refined crystal structure of the potato inhibitor complex of carboxypeptidase A at 2.5 Å resolution," *J. Mol. Biol.*, vol. 160, no. 3, pp. 475–498, 1982.
- [82] W. Lamine *et al.*, "Unexpected Structure of a Helical N4-Schiff-Base Zn (II) Complex and Its Demetallation: Experimental and Theoretical Studies," *ChemPhysChem*, vol. 19, no. 21, pp. 2938–2946, 2018.
- [83] C. J. T. De Grotthuss, "Memoir on the decomposition of water and of the bodies that it holds in solution by means of galvanic electricity," *Biochim. Biophys. Acta (BBA)-Bioenergetics*, vol. 1757, no. 8, pp. 871–875, 2006.
- [84] D. Marx, "Proton transfer 200 years after von Grotthuss: Insights from ab initio simulations," *ChemPhysChem*, vol. 7, no. 9, pp. 1848–1870, 2006.
- [85] M. Tuckerman, K. Laasonen, M. Sprik, and M. Parrinello, "Ab initio molecular dynamics simulation of the solvation and transport of hydronium and hydroxyl ions in water," *J. Chem. Phys.*, vol. 103, no. 1, pp. 150–161, 1995.
- [86] N. Mardirossian and M. Head-Gordon, "Thirty years of density functional theory in computational chemistry: an overview and extensive assessment of 200 density functionals," *Mol. Phys.*, vol. 115, no. 19, pp. 2315–2372, 2017.
- [87] B. Chan, A. T. B. Gilbert, P. M. W. Gill, and L. Radom, "Performance of density functional theory procedures for the calculation of proton-exchange barriers: Unusual behavior of M06-type functionals," *J. Chem. Theory Comput.*, vol. 10, no. 9, pp. 3777–3783, 2014.

- [88] A. Karton, R. J. O'Reilly, and L. Radom, "Assessment of theoretical procedures for calculating barrier heights for a diverse set of water-catalyzed proton-transfer reactions," *J. Phys. Chem. A*, vol. 116, no. 16, pp. 4211–4221, 2012.
- [89] A. Karton, R. J. O'Reilly, B. Chan, and L. Radom, "Determination of Barrier Heights for Proton Exchange in Small Water, Ammonia, and Hydrogen Fluoride Clusters with G4 (MP2)-Type, MPn, and SCS-MPn Procedures_ A Caveat," *J. Chem. Theory Comput.*, vol. 8, no. 9, pp. 3128–3136, 2012.333